Accurate Rectifier Characterization and Improved Modeling of Constant Power Load Wireless Power Transfer Systems

Jingdong Sun, *Student Member, IEEE*, Jonghyun Cho, *Member, IEEE*, Anfeng Huang, *Student Member, IEEE*, Hongseok Kim, *Member, IEEE*, and Jun Fan, *Fellow, IEEE*

***Abstract*—Wireless power transfer (WPT) is an emerging technology deployed for a wide range of applications. Various design challenges need to be addressed at both circuit and system levels. However, the conventional modeling methods either require impractical assumptions or only focus on the coil-to-coil part. This article presents a system-level model for WPT applications, including all the critical interior blocks, such as power amplifier, transmitter coil, receiver coil, matching networks, and rectifier. An accurate characterization method is proposed to obtain the rectifier impedance as a realistic load condition. Then, through frequency harmonic analysis, the power capabilities along the power flow path are analytically derived for both the fundamental and higher order harmonic components. The system efficiency and the power loss at each block can be accurately estimated. As a result, this model can not only optimize the system performance, but also help improve the thermal design for WPT products. With the assistance of this improved model, a practical design methodology is introduced to optimize the system parameters. An experimental prototype is built to validate the proposed model and the design methodology. Good correlations are observed between the calculations and experiments in both the time-domain and frequency-domain results.**

***Index Terms*—Analytical modeling, impedance analysis, inductive power transfer, rectifier characterization, system optimization.**

I. INTRODUCTION

WIRELESS power transfer (WPT) is an emerging technology that brings great convenience to charging a large variety of electronic devices. It has been widely deployed for domestic and industrial applications, including cell phones, home electronics, medical implants, and electric vehicles [1]–[4]. These applications usually have different requirements on power level, efficiency, physical size, and operating frequency. WPT standards, such as Qi from Wireless Power Consortium [5] and J2954 from the Society of Automotive Engineers [6], have been proposed to improve the interoperability and the safety protection of WPT applications.

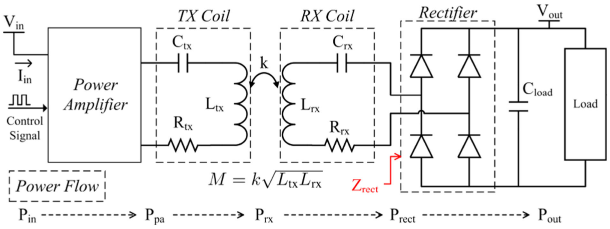

Fig. 1. Typical WPT system with the SS topology.

In addition to the standards and regulations, it is crucial to minimize the power loss and improve the efficiency of WPT systems, since the dissipated heat of devices may cause potential safety issues and throttle the charging performance. There are three major challenges in designing a power efficient WPT system. First, it remains an unresolved question to achieve the optimal efficiency at the system level. As shown in Fig. 1, a typical WPT system is formed by multiple blocks, including the power amplifier, the magnetic coils, the matching networks, and the rectifier. It is worth noting that the optimal configuration of a single block may not correspond to the peak efficiency of the entire system. Second, the power loss of each block in a WPT system needs to be estimated accurately. Because of the increasing power levels, the thermal design becomes more important for the electronic products. An effective thermal design needs to account for not only the end-to-end total loss, but also the dissipated power at each block along the power flow path. Third, there are no practical methodologies to simultaneously optimize multiple system parameters, such as the coil matching capacitance, the operating frequency, and the input voltage level. The conventional trial-and-error method requires extensive measurements on a prototype system, which is time-consuming and expensive. These challenges limit the performance for a wide range of WPT applications, including the cell phones and electric vehicles [3]. To overcome these challenges, an accurate system-level model is desired to conduct the global optimization and loss estimation for all the blocks in a WPT system.

Manuscript received August 22, 2019; revised November 13, 2019; accepted December 17, 2019. Date of publication December 19, 2019; date of current version April 22, 2020. This work was supported in part by the National Science Foundation under Grant IIP-1440110. Recommended for publication by Associate Editor M. Ponce-Silva. *(Corresponding author: Jun Fan.)*

J. Sun, A. Huang, H. Kim, and J. Fan are with the Electromagnetic Compatibility Laboratory, Missouri University of Science and Technology, Rolla, MO 65409 USA (e-mail: sunjing@mst.edu; ah4d8@mst.edu; kimhong@mst.edu; jfan@mst.edu).

J. Cho was with the Electromagnetic Compatibility Laboratory, Missouri University of Science and Technology, Rolla, MO 65409 USA. He is now with Rambus Inc., Sunnyvale, CA 94089 USA (e-mail: jcho@rambus.com).

Color versions of one or more of the figures in this article are available online at http://ieeexplore.ieee.org.

Digital Object Identifier 10.1109/TPEL.2019.2961359

Over the past few decades, various studies have been carried out to investigate WPT designs at both coil and system levels [7]–[12]. Among these studies, a magnetic coil design methodology for the WPT system was presented in [7]. In addition to magnetic coils, matching networks and other system parameters are also critical to maximize efficiency. In [8] and [9], the power transfer capability was analyzed under different matching topologies for the coupled coils. However, the output load of the coils was assumed to be purely resistive, which is impractical because the nonlinear rectifier device may contribute reactance components to the load in real WPT systems. The effects of rectifier input impedance were discussed in [10] and [11]. However, the authors in [10] only focused on the resonant condition and ignored the case when nonzero line impedance is present at the ac side of the rectifier. In addition, the rectifier impedance was obtained from PSPICE simulations, but the PSPICE model may be unavailable for many devices because of the lack of support or confidential concerns. In [11], an analytical model of the rectifier impedance was established for the positive half-cycles, but it neglected the nonlinearity caused by the line-commutation process. Zhang *et al.* presented analytical expressions of coil efficiency with both frequency and voltage tuning [12]. The derivations were based on the first harmonic approximation (FHA), which becomes inaccurate when the operation condition is not at the resonant frequency [13]. Other conditions from the existing WPT products also make FHA inaccurate, such as the low-voltage operation of the cell phone wireless charger, the low power charging mode that causes the loaded quality factor decreasing [14], and the frequency splitting and bifurcation phenomena due to high coupling coefficient [15].

This article aims to provide a comprehensive discussion on the system-level modeling for kilohertz WPT applications. The limitations of the existing models are investigated based on circuit-level simulations in Section II. To overcome these issues, an accurate characterization method for the rectifier is proposed in Section III. It provides a feasible solution to obtain the rectifier impedance, which is included as a realistic load condition for the improved WPT system model in Section IV. Using this model, a design methodology is introduced to determine the optimized parameters for a WPT system. Then, an experimental prototype is implemented to validate the proposed model and the design methodology in Section V. Finally, Section VI concludes this article.

II. TOPOLOGY AND PREINVESTIGATION

A typical WPT system (see Fig. 1) consists of four blocks: 1) the power amplifier, to convert dc input voltage V_{in} and current I_{in} to ac power, which is commonly implemented by half-bridge or full-bridge topology; 2) the transmitter (TX) coil with self-inductance L_{tx} and matching capacitance C_{tx}; 3) the receiver (RX) coil with self-inductance L_{rx} and matching capacitance C_{rx}; and 4) the rectifier, to inversely regulate ac power to dc output voltage V_{out}.

In this article, the series–series (SS) matching topology is used. Other matching topology, such as parallel–series, series–parallel, and parallel–parallel, can be derived in a similar manner [8], [9]. For the remaining parameters in Fig. 1, R_{tx} and R_{rx} are the equivalent series resistances (ESRs) of the coils and matching capacitors. k is the coupling coefficient of the coupled magnetic coils. Then, the mutual inductance can be expressed as $M = k\sqrt{L_{\text{tx}}L_{\text{rx}}}$. C_{load} is the smoothing capacitor at the rectifier's output. It is a common practice for WPT applications to add sufficiently large C_{load} to stabilize the output voltage, so the output voltage ripple can be neglected. Z_{rect} is the input impedance seen at the rectifier input port. Fig. 1 also illustrates the power flow of a WPT system, including TX input power P_{in}, power amplifier output P_{pa}, transferred power to the RX side P_{rx}, rectifier input power P_{rect}, and RX output power P_{out}. The rated output power is typically specified as a requirement in the early design stage, and the output voltage is constant in WPT systems [16]–[18]. For the design purpose of efficiency optimization under the maximum output power, this article focuses on the constant power load (CPL) condition with fixed output voltage.

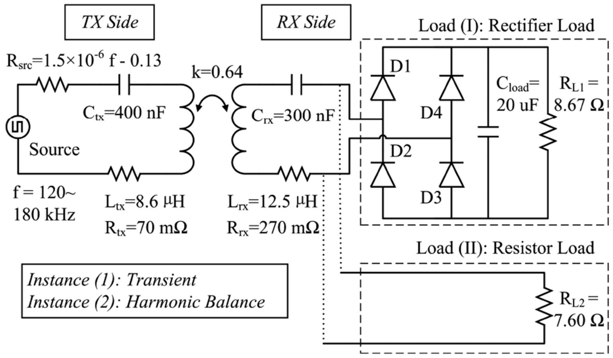

Fig. 2. Diagram of the circuit model for preinvestigation. Two simulation instances are defined for the time-domain and frequency-domain comparison.

To investigate the limitations of assumptions used in the existing methods, a circuit model is built in an RF simulator, Keysight Advanced Design Systems, based on the WPT system with the SS topology. As some WPT models only focused on the coil-to-coil part, the system efficiency is compared with the coil-only efficiency to show the significance of other blocks in the system. Then, the inaccuracy of FHA is investigated by the comparison between the time-domain and frequency-domain results. Finally, by applying different load conditions to the RX coil's output, the simulations demonstrate that inaccurate estimation of the efficiency can be caused by the pure resistive load assumption. Therefore, it is important to model the WPT system with a realistic load impedance.

The configuration of this circuit model is depicted in Fig. 2. The value of each element is chosen based on a Qi-standard cell phone WPT system. This model can be simulated in both time and frequency domains by different simulation instances. On the TX side, the power amplifier is simplified to a trapezoidal-wave voltage source. The amplitude of this voltage source is between $-V_{\text{in}}$ and V_{in}; the operating frequency is f. A frequency-dependent equivalent resistor R_{src} is used to account for the power loss caused by the power amplifier. The function of R_{src} is determined by fitting the simulated power loss to the measured

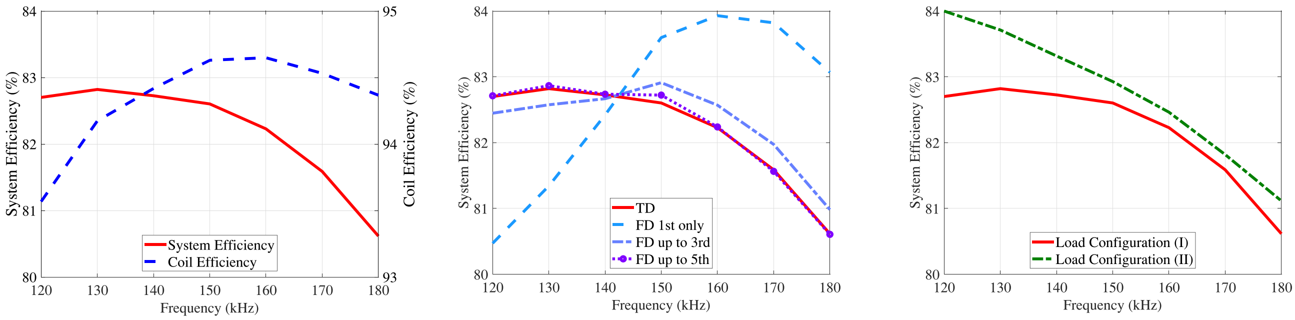

(a)

(b)

(c)

Fig. 3. Simulation results of the circuit model. (a) Comparison between system and coil-to-coil efficiencies. (b) Comparison of efficiencies in time and frequency domains. "TD" is the time-domain result. "FD 1st only" implies that only fundamental frequency is considered. "FD up to 3rd" includes up to the third-order harmonics. And "FD up to 5th" includes up to the fifth-order harmonics. (c) Comparison of the system efficiencies under two load configurations.

power loss of an existing power amplifier. Even though the equivalent resistor simplification cannot accurately model the loss of the power amplifier, it is sufficient to preinvestigate the limitations of the existing methods. A more rigorous modeling method is discussed in Section IV. On the RX side, the output power is fixed at 8 W. The CPL condition is satisfied by tuning V_{in} and f. Two load configurations are applied: (I) a full-bridge rectifier (D1–D4) with the load resistor R_{L1}; and (II) a pure resistor load R_{L2} directly connected to the RX matching network. To ensure similar output power levels for the two load configurations, R_{L2} is converted from R_{L1} based on the approximated effective resistance equation [14]

$$R_{\mathrm{L2}} = \frac{8R_{\mathrm{L1}}}{\pi^2}\left(1 + \frac{2V_{\mathrm{fw}}}{V_{\mathrm{out}}}\right) \tag{1}$$

where $V_{\mathrm{fw}} = 0.34$ V is the forward voltage of the rectification diode, and $V_{\mathrm{out}} = 8.33$ V is the rectifier output voltage.

A. Investigation of System and Coil Efficiency

Fig. 3(a) compared the system and coil efficiencies at different frequencies using the load configuration (I). The system and coil efficiencies, η_{sys} and η_{coil}, were calculated as

$$\eta_{\mathrm{sys}} = \frac{P_{\mathrm{out}}}{P_{\mathrm{in}}} \cdot 100\% \tag{2}$$

$$\eta_{\mathrm{coil}} = \frac{P_{\mathrm{rect}}}{P_{\mathrm{pa}}} \cdot 100\% \tag{3}$$

where P_{in} and P_{out} are the input and output powers, respectively, and P_{pa} and P_{rect} are the power amplifier output and rectifier input powers, respectively.

Note that the peak system efficiency is achieved at a lower frequency compared with the peak coil efficiency. This implies that the TX and RX coil blocks are not the only factors determining the efficiency for a WPT system. Other blocks also have significant contributions; one important loss term related to frequency is the MOSFET switching loss of the power amplifier [19]. As the frequency increases from 120 to 180 kHz, the simulated loss of the power amplifier reaches up to 583 mW. In addition, the design of coil's matching network also affects the current flowing through all the blocks, which could affect the loss of the power amplifier and the rectifier. In the simulations and optimizations for real-world WPT applications, a system-level model is preferred over a coil-to-coil only model.

B. Investigation of Harmonic Frequency

The simulated system efficiencies in the time and frequency domains, using the load configuration (I), were compared in Fig. 3(b). For the time-domain simulation, the steady-state voltage and current waveforms were directly multiplied in a unit time step to calculate the input and output powers. The system efficiency in the time domain was obtained based on (2). For the frequency-domain simulation, with the dc output power fixed to 8 W, the input power carried by each frequency component was calculated individually by the magnitudes and phase difference of the simulated voltage and current. Then, the system efficiencies in the frequency domain were determined using the input power of the fundamental frequency only ("FD 1st only"), the input power including up to the third-order harmonics ("FD up to 3rd"), and the input power including up to the fifth-order harmonics ("FD up to 5th").

As shown in Fig. 3(b), only at the crossing point, the efficiency calculated by the fundamental frequency component can match with the time-domain efficiency. It is because the input power of higher order harmonics is zero due to the 90° phase angle between the voltage and current, and only the fundamental frequency component carries the input power. With the increasing offset to this condition, the difference of the efficiencies using the fundamental frequency component and using the time-domain component becomes larger. It implies that FHA is not applicable, and higher order harmonic components should not be neglected. The inaccuracy of FHA is mainly due to two reasons. First, the voltage source of a real WPT system is not sinusoidal. Second, the nonlinearity of the rectifiers is not taken into consideration in FHA [20]. Therefore, a valid WPT model should have the capability to characterize the power distributed at both fundamental frequency and higher order harmonics. The waveform in a WPT system typically has a 50% duty cycle, so the power carried by even harmonics is negligible. For all practical purposes, the fundamental, third-order, and fifth-order harmonic components are the most critical terms in a WPT model.

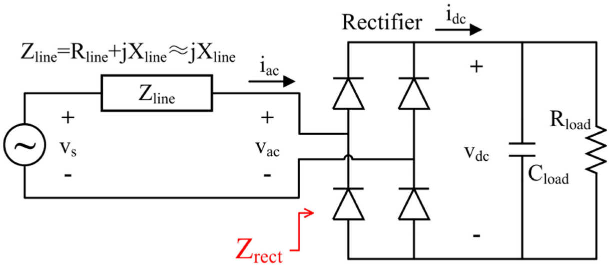

Fig. 4. Circuit model of a full-wave diode rectifier.

C. *Investigation of Rectifier Impedance*

The system efficiencies of two load configurations were compared in Fig. 3(c). Since the circuit of the load configuration (II) has no rectifier, to maintain the validity of this comparison, the output power in this case was estimated using an artificial full-bridge rectifier with a forward voltage V_{fw} of the rectification diode

$$P_{\text{out}}^{\text{Load (II)}} = P_{\text{L2}} \cdot \frac{V_{\text{out}}}{V_{\text{out}} + 2V_{\text{fw}}} \tag{4}$$

where P_{L2} is the simulated power at R_{L2}, and V_{fw} and V_{out} are defined the same as (1). Then, the system efficiency can be calculated based on (2).

In load configuration (I), the simulated rectifier reactance varies from 0 to 1.34 Ω at different frequencies. The nonzero reactance at the RX side could affect the reflected impedance at the TX side and change the coil efficiency. With the absence of this rectifier reactance, in load configuration (II), the coil efficiency has less variation at different frequencies. As a result, the pure resistor load model gives a misleading estimation for the system efficiency and the optimal operation point. Therefore, a realistic load configuration is important to accurately model the efficiency in WPT systems. Both real and imaginary parts of the load impedance should be included in the model. It is also desirable to develop a practical characterization method for the provided rectifier diodes or ICs, in order to obtain the accurate impedance under various conditions.

III. ACCURATE RECTIFIER CHARACTERIZATION

The rectifier is a common nonlinear device in ac–dc power systems. The nonlinearity of the rectifier is mainly caused by the parasitic of the rectification diode [21] and the line-commutation process [22]. Fig. 4 depicts the circuit model of a full-wave diode rectifier. The source voltage is denoted as v_{s}. At the dc output port of the rectifier, there are output voltage v_{dc} and output current i_{dc}. The dc component of i_{dc} is I_{d}. The load resistance and the smoothing capacitor are R_{load} and C_{load}, respectively. At the input port of the rectifier, there are ac voltage v_{ac} and ac current i_{ac}. The ac-side line impedance is defined as $Z_{\text{line}} = R_{\text{line}} + jX_{\text{line}}$. The line resistance R_{line} will cause the voltage drop from the source to the rectifier input. Since its value is determined by the ac resistance of the coils and the ESR of the matching capacitors, which is typically tens of milliohm, R_{line} can be neglected as a common practice. X_{line} is calculated by the line impedance of the RX side and the reflected impedance from the TX side as

$$X_{\text{line}} = \omega L_{\text{rx}} - \frac{1}{\omega C_{\text{rx}}} - \frac{(\omega M)^2}{\left(\omega L_{\text{tx}} - \frac{1}{\omega C_{\text{tx}}}\right)} \tag{5}$$

where L_{tx} and L_{rx} are the TX and RX coil inductances, respectively, C_{tx} and C_{rx} are the TX and RX matching capacitances, respectively, M is the mutual inductance between two coils, and ω is the angular operating frequency. Depending on the coil inductance, matching network, and operating frequency, nonnegligible X_{line} may present at the input of the rectifier.

Based on the small-signal analysis [22]–[25], the source voltage v_{s} consists of a sinusoidal wave v_1 and a small-signal perturbation Δv_{p}: $v_{\text{s}} = v_1 + \Delta v_{\text{p}}$. The amplitude of Δv_{p} is much smaller than that of v_1: $|v_1| = V_1, |\Delta v_{\text{p}}| = V_{\text{p}}$ with $V_{\text{p}} \ll V_1$. The rectifier impedance Z_{rect} can be expressed as follows (see the Appendix for the full derivation):

$$Z_{\text{rect}} = \frac{(\Delta v_{\text{p}} - \Delta S\ I_{\text{d}}\ Z_{\text{line}})\,(2Z_{\text{line}} + R_{\text{load}})}{2S\ \Delta S\ v_1 + S^2\ \Delta v_{\text{p}} - 3S^2\ \Delta S\ I_{\text{d}}\ Z_{\text{line}}} \tag{6}$$

where S and ΔS are the nonlinear switching functions; S accounts for the line-commutation process and the parasitic of the rectification diode [22], and ΔS accounts for the change of nonlinearity caused by the input perturbation [24]. v_1 and v_{p} can be further expanded into the complex forms at the perturbation frequency with the amplitudes V_1 and V_{p}, respectively. The nonlinearity of perturbation ΔS is proportional to Δv_{p} with the same amplitude, so V_{p} is canceled. As a result, Z_{rect} is a function of the operating frequency, the input voltage amplitude V_1, the dc load current I_{d}, the load impedance R_{load}, and the input line impedance Z_{line}.

With the focus on the main nonlinear behaviors caused by the line-commutation process and the parasitic of the rectification diode ($S \neq 0, \Delta S = 0$), (6) can be simplified to (7). In addition, the line resistance R_{line} can be neglected as a common practice, so $Z_{\text{line}} = jX_{\text{line}}$

$$Z_{\text{rect}}|_{\Delta S=0} = \frac{2jX_{\text{line}} + R_{\text{load}}}{S^2}. \tag{7}$$

It implies that the rectifier impedance is mainly affected by X_{line} and load impedance R_{load}. With the CPL condition applied to the WPT systems, X_{line} becomes an effective criterion to characterize the rectifier impedance.

As discussed in [22], a standard sign function is used to represent the line-commutation process of the nonlinear switching function S. However, the analytical model described in this article is based on the assumption that no input line impedance is present at the ac side of the rectifier. It is not applicable to the kilohertz WPT system because X_{line} is commonly nonnegligible when the system is operating in an off-resonance condition. Another method to obtain the rectifier impedance is from the circuit simulation, where users need to correctly set all the parameters for the target device under simulation. Some electrical parameters, such as forward voltage drop (V_{fw}) and reverse break down voltage (B_{v}), are accessible from the datasheet. However, some physical parameters, such as junction grading coefficient (m), emission coefficient (N), saturation current (I_{s}), parasitic

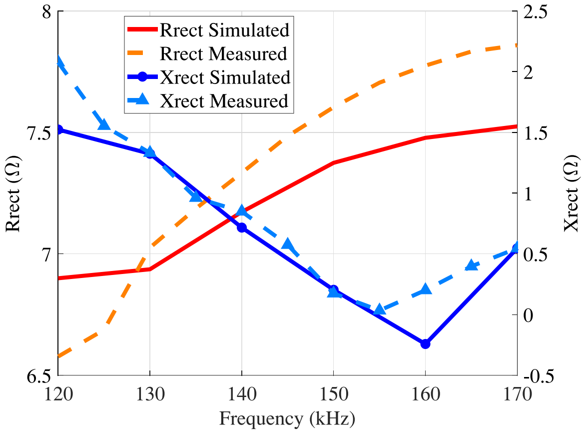

Fig. 5. Comparison of simulated and measured rectifier impedance. Only fundamental frequency component is considered in this figure. The part number of rectification diode is DIODES SBR3U40P1. $m = 0.333$, $N = 2$, $I_s = 1.8e^{-3}$ A. $R_s = 34$ mΩ, $C_{jo} = 80$ pF, $T_t = 0$ ns, and $B_v = 40$ V.

resistance (R_s), zero-bias junction capacitance (C_{jo}), and transit time (T_t), are either unavailable or require complicated calculations based on the figures in the datasheet. To investigate the accuracy of the circuit simulation for the rectifier impedance, a full-bridge rectifier using four Schottky diodes (SBR3U40P1) was simulated. In spite of the specified parameters, the unavailable parameters, including M, N, and T_t, were set using the recommended values from [26]. Other parameters, such as I_s, R_s, and C_{jo}, were calculated or extracted based on the typical characteristics and capacitance figures from the datasheet. The operating frequency varied from 120 to 170 kHz, The coil inductance, matching networks, and X_{line} were maintained the same for both simulation and measurement setups at each frequency. The comparison between the measured and simulated results is depicted in Fig. 5. The rectifier impedance (Z_{rect}) is compared by its real and imaginary parts (R_{rect} and X_{rect}), respectively:

$$Z_{\text{rect}} = R_{\text{rect}} + jX_{\text{rect}}. \tag{8}$$

Large discrepancies are shown between the simulated and measured rectifier impedances. There are mainly two reasons for the inaccurate results. First, some parameters are not specified in the datasheet; setting recommended values based on user's experiences or extracting values from the figures will introduce errors. Second, the testing condition in the datasheet may not be the same as the operating condition in measurement. Thus, the parameters may change in a real WPT system. In sum, the analytical equation and circuit simulation are not capable of obtaining the rectifier impedance accurately.

In this article, a measurement-based characterization method is proposed for the rectifier. It provides the rectifier impedance and efficiency under the real operating condition. The characterization setup is illustrated in Fig. 6. In practice, the load of the rectifier may consist of a dc–dc voltage regulator charging a battery. The dc–dc voltage regulator, such as buck or buck–boost converter, can be modeled as an equivalent resistor [27], [28]. Therefore, a resistive load R_{load} is used to represent a subcircuit feeding the actual physical electric load of the rectifier [29]. A differential voltage probe and a current probe are applied to the input port of the rectifier. The ac input voltage and current waveforms are measured by the oscilloscope in the time domain. Then, all stored data are processed by fast Fourier transformation (FFT) to provide the impedance in the frequency domain. There are several advantages in applying the time-domain measurements. First, the phase information is accessible by using a less expensive instrument (i.e., an oscilloscope instead of a vector network analyzer). Also, with the relatively high signal-to-noise ratio signals operating in the kilohertz frequency range, the phase information could be obtained without the down mixing method. In addition, the measurement time is reduced, since a single-shot waveform in the time domain contains the complete information in the frequency range of interest (both fundamental and higher order harmonic components).

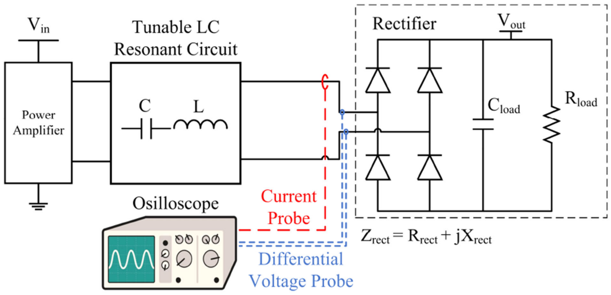

Fig. 6. Measurement-based rectifier impedance characterization setup.

TABLE I

COIL PARAMETERS FOR CHARACTERIZATION AND VALIDATION SETUPS

Coil Parameter	Generic Coil Module for Characterization	WPT System Coil for Validation
L_{tx}	7.90 μH	8.58 μH
L_{rx}	7.90 μH	12.52 μH
C_{tx}	400 nF	400 nF
C_{rx}	100, 200, 300, 400 nF	200 nF
k	0.58	0.63

The tunable LC resonant circuit is implemented to vary X_{line}. It is preferable to use a generic coil-to-coil module because of three main reasons. First, the line impedance X_{line} can be easily changed by the matching capacitance and the topology. Second, the scenario for characterization is close to the real WPT system, so it can achieve good coverage of the interested parameter range. Third, there is no additional hardware or cost. The parameters of the generic coil used in the rectifier characterization are described in Table I. The line impedance X_{line} is tuned by varying the operating frequency and RX matching capacitance C_{rx}. The characterization results were validated by a real WPT system with a different set of coils.

In Fig. 7, the real and imaginary parts of the rectifier impedance (R_{rect} and X_{rect}) are characterized separately. The circular dots are the characterization points using the generic coil module. The solid line is the fitted impedance curve based on the characterization points. The triangle dots are the measured rectifier impedance of a real WPT system. Both R_{rect} and X_{rect}

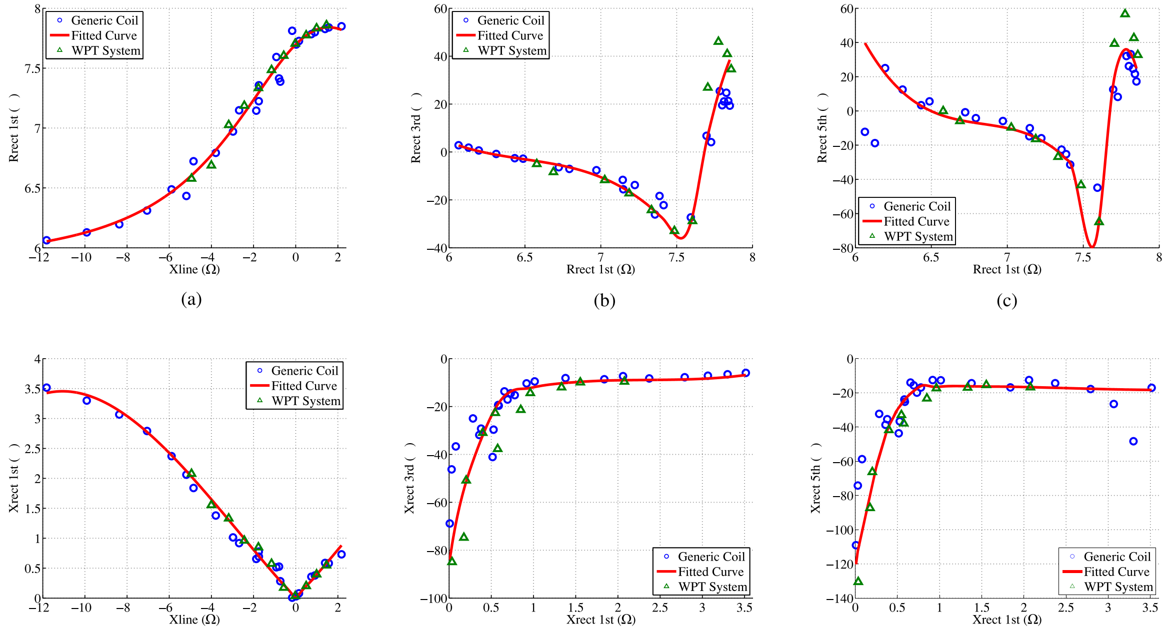

(a) (b) (c)

(d) (e) (f)

Fig. 7. Rectifier impedance characterization and validation results. The part number of the rectification diode is DIODES SBR3U40P1. $V_{\text{out}} = 8.3$ V, $P_{\text{out}} = 8$ W, $Z_{\text{load}} = 8.67\ \Omega$, and operating frequency is 120–180 kHz. (a) R_{rect} fundamental frequency versus X_{line}. (b) R_{rect} third-order harmonic versus fundamental. (c) R_{rect} fifth-order harmonic versus fundamental. (d) X_{rect} fundamental frequency versus X_{line}. (e) X_{rect} third-order harmonic versus fundamental. (f) X_{rect} fifth-order harmonic versus fundamental.

at the fundamental frequency have strong correlation with X_{line} [see Fig. 7(a) and (d)]. Then, the impedance at the third- and fifth-order harmonics can be further predicted by R_{rect} and X_{rect} at the fundamental frequency [see Fig. 7(b), (c), (e), and (f)]. Thus, Z_{rect} can be accurately obtained in terms of its most critical frequency components for a WPT model.

The rectifier efficiency (η_{rect}) is mainly affected by the forward voltage drop of the rectification diode, the output voltage of the rectifier, and the power level. This article focuses on the CPL WPT system, where the output power and voltage are fixed. The characterization is also conducted on a provided rectifier with the predetermined forward resistance property. So, η_{rect} is expected to be constant under different operation conditions. The measured η_{rect} in both characterization and validation setups was between 93.6% and 94.0%. For simplicity, the averaged value 93.8% was chosen as the characterized rectifier efficiency.

Currently, the characterization curves are fitted using polynomial and rational functions, which are sufficient for kilohertz WPT systems. However, certain discrepancies were observed at higher frequency harmonics [see Fig. 7(c) and (f)]. It implied that more complicated fitting or data training techniques should be applied for the WPT system with higher operating frequency (megahertz or above). This part of work is beyond the scope of this article and will be discussed in future studies.

IV. IMPROVED MODELING AND DESIGN METHODOLOGY

In this section, an improved WPT system model is demonstrated with the characterized rectifier impedance. This model is established based on the premise that all the blocks of a target WPT system are provided. Then, the coil parameters, the impedance and the efficiency of the rectifier, and the parasitic effects of the power amplifier can be obtained in advance (see Table II: Known Parameters). The goal of this method is to optimize the matching network, input voltage, and operating frequency (see Table II: Design Parameters), in order to obtain the peak system efficiency and accurate power loss of each block (see Table II: Target Outputs). A practical design methodology is introduced to optimize these system parameters.

TABLE II
CATEGORIES OF THE WPT SYSTEM MODEL PARAMETERS

Category	Parameter	Description
Known Parameters	$L_{\text{tx}}, L_{\text{rx}}, R_{\text{tx}}, R_{\text{rx}}, k$	Coil inductance and ac resistances, coupling coefficient
	$R_{\text{rect}}, X_{\text{rect}}, \eta_{\text{rect}}$	Rectifier impedance and efficiency
	$t_{\text{f}}, t_{\text{dead}}, V_{\text{d}}, R_{\text{on}}$	Power amplifier fall/dead times, MOSFET body-diode forward voltage and on-resistance
Design Parameters	V_{in}	TX dc input voltage
	$\omega = 2\pi f$	Operation frequency
	$C_{\text{tx}}, C_{\text{rx}}$	Capacitance of the TX and RX matching networks
Target Outputs	$P_{\text{in}}, P_{\text{pa}}, P_{\text{rx}}, P_{\text{rect}}$	Powers at the block interfaces
	η_{sys}	System efficiency

A. Improved Modeling of the WPT System

A typical WPT system is formulated in Fig. 8. As discussed in Section II, the power amplifier at the TX side can be simplified to

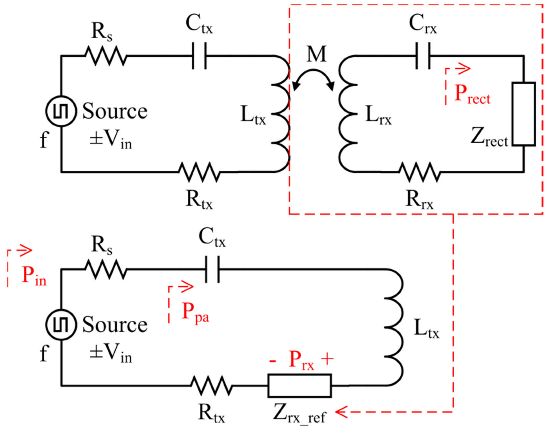

Fig. 8. Formulation for the improved modeling of the WPT system.

a trapezoidal-wave voltage source. Since the rising/falling time of the input voltage waveform (typically tens of nanoseconds) is relatively small compared with the switching period (several microseconds for a kilohertz WPT system), the input source can be modeled as a square wave with additional losses due to the transition edges. The original dc input voltage V_{in} then becomes the amplitude of this square wave. R_{s} is related to the ON-resistance R_{on} of the MOSFET in the power amplifier. It leads to the voltage drop along the power flow path and affects the back-end blocks. For a half-bridge power amplifier, $R_{\text{s}} = R_{\text{on}}$. For a full-bridge power amplifier, $R_{\text{s}} = 2R_{\text{on}}$. The rectifier impedance at the RX side is Z_{rect}, which is included in this model as a realistic load condition. The characterization method for Z_{rect} and the rectifier efficiency η_{rect} is introduced in Section III.

Based on the standard mutual inductance coupling transfer model, the RX-side circuits can be represented as a reflected impedance $Z_{\text{rx\_ref}}$ at the TX side

$$Z_{\text{rx\_ref}} = \frac{(\omega M)^2}{R_{\text{rx}} + j\omega L_{\text{rx}} + \frac{1}{j\omega C_{\text{rx}}} + Z_{\text{rect}}}. \tag{9}$$

Combining (8) and (9), $Z_{\text{rx\_ref}}$ can be represented as

$$\begin{aligned} Z_{\text{rx\_ref}} &= \frac{(\omega M)^2}{(R_{\text{rx}} + R_{\text{rect}}) + j\left(\omega L_{\text{rx}} - \frac{1}{\omega C_{\text{rx}}} + X_{\text{rect}}\right)} \\ &= \left[\frac{(\omega M)^2 (R_{\text{rx}} + R_{\text{rect}})}{(R_{\text{rx}} + R_{\text{rect}})^2 + \left(\omega L_{\text{rx}} - \frac{1}{\omega C_{\text{rx}}} + X_{\text{rect}}\right)^2}\right] \\ &\quad + j\left[\frac{-(\omega M)^2 \left(\omega L_{\text{rx}} - \frac{1}{\omega C_{\text{rx}}} + X_{\text{rect}}\right)}{(R_{\text{rx}} + R_{\text{rect}})^2 + \left(\omega L_{\text{rx}} - \frac{1}{\omega C_{\text{rx}}} + X_{\text{rect}}\right)^2}\right] \\ &\triangleq R_{\text{rx\_ref}} + jX_{\text{rx\_ref}} \end{aligned} \tag{10}$$

where $R_{\text{rx\_ref}}$ and $X_{\text{rx\_ref}}$ are the real and imaginary parts of the reflected impedance, respectively.

Note that (10) is applicable to one single frequency. In order to take multiple harmonic frequencies into consideration, a superscript (n) is introduced into each notation to denote the index of the harmonic frequency. For example, the variables $X^{(1)}$, $X^{(3)}$, and $X^{(5)}$ are the fundamental, third-order, and fifth-order frequency harmonics, respectively. Then, $R_{\text{rx\_ref}}$ and $X_{\text{rx\_ref}}$ can be represented as

$$\begin{cases} R_{\text{rx\_ref}}^{(n)} = \dfrac{(n\omega_0 M)^2 \left(R_{\text{rx}}^{(n)} + R_{\text{rect}}^{(n)}\right)}{\left(R_{\text{rx}}^{(n)} + R_{\text{rect}}^{(n)}\right)^2 + \left(n\omega_0 L_{\text{rx}} - \frac{1}{n\omega_0 C_{\text{rx}}} + X_{\text{rect}}^{(n)}\right)^2} \\ X_{\text{rx\_ref}}^{(n)} = \dfrac{-(n\omega_0 M)^2 \left(n\omega_0 L_{\text{rx}} - \frac{1}{n\omega_0 C_{\text{rx}}} + X_{\text{rect}}^{(n)}\right)}{\left(R_{\text{rx}}^{(n)} + R_{\text{rect}}^{(n)}\right)^2 + \left(n\omega_0 L_{\text{rx}} - \frac{1}{n\omega_0 C_{\text{rx}}} + X_{\text{rect}}^{(n)}\right)^2} \end{cases} \tag{11}$$

where ω_0 is the fundamental component of the operating frequency.

The total load impedance of the power amplifier at the TX side is denoted as Z_{pa}. Similar as the reflected impedance, Z_{pa} can be represented with the real and imaginary terms

$$Z_{\text{pa}}^{(n)} \triangleq R_{\text{pa}}^{(n)} + jX_{\text{pa}}^{(n)}$$

where

$$\begin{cases} R_{\text{pa}}^{(n)} = R_{\text{s}} + R_{\text{tx}}^{(n)} + R_{\text{rx\_ref}}^{(n)} \\ X_{\text{pa}}^{(n)} = n\omega_0 L_{\text{tx}} - \frac{1}{n\omega_0 C_{\text{tx}}} + X_{\text{rx\_ref}}^{(n)}. \end{cases} \tag{12}$$

As the input source is modeled as a square wave. The power losses related to the transition edges are calculated separately. Using the Fourier transform, the input source of a square wave can be divided into multiple sinusoidal harmonics, with the amplitude of each harmonic being

$$V_{\text{s}}^{(n)} = \frac{C}{\pi} \frac{V_{\text{in}}}{n} \tag{13}$$

where C is a constant determined by the power amplifier's topology. For a half-bridge power amplifier, $C = 2$ as the switching voltage changes from 0 to V_{in}. For a full-bridge power amplifier, $C = 4$ as the switching voltage changes from $-V_{\text{in}}$ to V_{in}. With (13), the input power distributed on each harmonic component can be calculated as

$$\begin{aligned} P_{\text{in,cond}}^{(n)} &= \frac{1}{2}\left(V_{\text{s}}^{(n)}\right)^2 \frac{R_{\text{pa}}^{(n)}}{\left(R_{\text{pa}}^{(n)}\right)^2 + \left(X_{\text{pa}}^{(n)}\right)^2} \\ &= \frac{(CV_{\text{in}})^2}{2\pi^2 n^2} \frac{R_{\text{pa}}^{(n)}}{\left(R_{\text{pa}}^{(n)}\right)^2 + \left(X_{\text{pa}}^{(n)}\right)^2}. \end{aligned} \tag{14}$$

The time-domain input power is the sum of all the frequency harmonics

$$\begin{aligned} P_{\text{in,cond}} &= \sum_{n=1}^{\infty} P_{\text{in,cond}}^{(n)} \\ &= \frac{(CV_{\text{in}})^2}{2\pi^2} \sum_{n=1}^{\infty} \left[\frac{1}{n^2} \cdot \frac{R_{\text{pa}}^{(n)}}{\left(R_{\text{pa}}^{(n)}\right)^2 + \left(X_{\text{pa}}^{(n)}\right)^2}\right] \end{aligned} \tag{15}$$

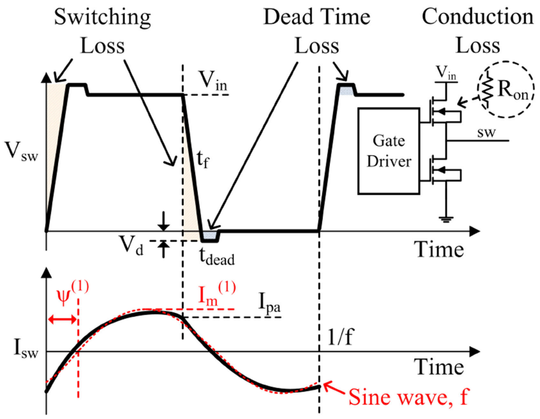

Fig. 9. Time-domain voltage and current waveforms at the switching node of a half-bridge power amplifier. The switching loss and dead time loss are depicted by the yellow- and blue-shaded areas, respectively. The red-dotted line is a sine wave with the fundamental frequency f.

where $R_{\text{pa}}^{(n)}$ and $X_{\text{pa}}^{(n)}$ are shown in (12). The full expansion of $P_{\text{in,cond}}$ is straightforward and will be omitted here.

Note that $P_{\text{in,cond}}$ only considers the conduction loss of the power amplifier. To model the total input power of the WPT system, the switching loss $P_{\text{loss,sw}}$ and the dead time loss $P_{\text{loss,dead}}$ of the power amplifier should also be included [30]

$$P_{\text{in}} = P_{\text{in,cond}} + P_{\text{loss,sw}} + P_{\text{loss,dead}}. \tag{16}$$

The switching loss and the dead time loss occur at the MOSFET ON–OFF transitions. For a zero-voltage-switched power amplifier, $P_{\text{loss,sw}}$ is mainly contributed by the turn-OFF switching losses of the high-side and low-side MOSFETs. And $P_{\text{loss,dead}}$ is caused by the current flowing through the body diodes during the excessive dead time after each transition. As shown in Fig. 9, $P_{\text{loss,sw}}$ and $P_{\text{loss,dead}}$ for a half-bridge power amplifier (one pair of high-side and low-side MOSFETs) can be approximated using simple time-domain figure calculations. For a full-bridge power amplifier, $P_{\text{loss,sw}}$ and $P_{\text{loss,dead}}$ need to be doubled compared with the half-bridge power amplifier

$$P_{\text{loss,sw}} = \begin{cases} V_{\text{in}} I_{\text{pa}} t_{\text{f}} f, & \text{half-bridge power amplifier} \\ 2V_{\text{in}} I_{\text{pa}} t_{\text{f}} f, & \text{full-bridge power amplifier} \end{cases} \tag{17}$$

$$P_{\text{loss,dead}} = \begin{cases} 2V_{\text{d}} I_{\text{pa}} t_{\text{dead}} f, & \text{half-bridge power amplifier} \\ 4V_{\text{d}} I_{\text{pa}} t_{\text{dead}} f, & \text{full-bridge power amplifier} \end{cases} \tag{18}$$

where t_{f} is the falling time of the ON–OFF transition. t_{dead} is the dead time after the rising/falling transitions. V_{d} is the forward voltage of the MOSFET body diode. V_{in} and f are the design parameters: input voltage and operating frequency. I_{pa} is the switching node current I_{sw} at the ON–OFF transition edge

$$I_{\text{pa}} = I_{\text{sw}}(t = t_{\text{on}\to\text{off}}). \tag{19}$$

I_{sw} is the composition of a sine wave with the operating frequency f and its higher order harmonics. The amplitude of each frequency component is denoted as $I_{\text{m}}^{(n)}$, which can be calculated as in [14]

$$I_{\text{m}}^{(n)} = V_{\text{s}}^{(n)} \frac{\cos\Psi^{(n)}}{R_{\text{pa}}^{(n)}} = \frac{CV_{\text{in}}}{\pi} \frac{\cos\Psi^{(n)}}{nR_{\text{pa}}^{(n)}} \tag{20}$$

$$I_{\text{sw}}(t) = \sum_{n=1}^{\infty} I_{\text{m}}^{(n)} \sin(2n\pi f t - \Psi^{(n)}) \tag{21}$$

where $\Psi^{(n)} = \tan^{-1}(X_{\text{pa}}^{(n)}/R_{\text{pa}}^{(n)})$ is the phase difference between voltage and current at the switching node.

Suppose that the MOSFET ON–OFF transition occurs at time $t_{\text{on}\to\text{off}} = 1/(2f)$. From (19)–(21), I_{pa} is calculated using the following formula:

$$\begin{aligned} I_{\text{pa}} &= \sum_{n=1}^{\infty} I_{\text{m}}^{(n)} \sin(n\pi - \Psi^{(n)}) \\ &= \frac{CV_{\text{in}}}{\pi} \sum_{n=1}^{\infty} \frac{V_{\text{s}}^{(n)} \cos\Psi^{(n)}}{nR_{\text{pa}}^{(n)}} \sin(n\pi - \Psi^{(n)}). \end{aligned} \tag{22}$$

Integrate I_{pa} into (17) and (18) to determine the $P_{\text{loss,sw}}$ and $P_{\text{loss,dead}}$, respectively. Finally, based on (16), the total input power of the WPT system P_{in} can be obtained.

The power flowing through the other blocks, such as the power amplifier, WPT coils, and rectifier, can be derived in a similar manner as

$$\begin{aligned} P_{\text{pa}} &= \sum_{n=1}^{\infty} P_{\text{pa}}^{(n)} = \sum_{n=1}^{\infty} \left(P_{\text{in,cond}}^{(n)} \frac{R_{\text{tx}}^{(n)} + R_{\text{rx\_ref}}^{(n)}}{R_{\text{pa}}^{(n)}} \right) \\ &= \frac{(CV_{\text{in}})^2}{2\pi^2} \sum_{n=1}^{\infty} \left[\frac{1}{n^2} \cdot \frac{R_{\text{tx}}^{(n)} + R_{\text{rx\_ref}}^{(n)}}{\left(R_{\text{pa}}^{(n)}\right)^2 + \left(X_{\text{pa}}^{(n)}\right)^2} \right] \end{aligned} \tag{23}$$

$$\begin{aligned} P_{\text{rx}} &= \sum_{n=1}^{\infty} P_{\text{rx}}^{(n)} = \sum_{n=1}^{\infty} \left(P_{\text{pa}}^{(n)} \frac{R_{\text{rx\_ref}}^{(n)}}{R_{\text{tx}}^{(n)} + R_{\text{rx\_ref}}^{(n)}} \right) \\ &= \frac{(CV_{\text{in}})^2}{2\pi^2} \sum_{n=1}^{\infty} \left[\frac{1}{n^2} \cdot \frac{R_{\text{rx\_ref}}^{(n)}}{\left(R_{\text{pa}}^{(n)}\right)^2 + \left(X_{\text{pa}}^{(n)}\right)^2} \right] \end{aligned} \tag{24}$$

$$\begin{aligned} P_{\text{rect}} &= \sum_{n=1}^{\infty} P_{\text{rect}}^{(n)} = \sum_{n=1}^{\infty} \left(P_{\text{rx}}^{(n)} \frac{R_{\text{rect}}^{(n)}}{R_{\text{rx}}^{(n)} + R_{\text{rect}}^{(n)}} \right) \\ &= \frac{(CV_{\text{in}})^2}{2\pi^2} \sum_{n=1}^{\infty} \left[\frac{1}{n^2} \frac{R_{\text{rx\_ref}}^{(n)}}{\left(R_{\text{pa}}^{(n)}\right)^2 + \left(X_{\text{pa}}^{(n)}\right)^2} \frac{R_{\text{rect}}^{(n)}}{R_{\text{rx}}^{(n)} + R_{\text{rect}}^{(n)}} \right]. \end{aligned} \tag{25}$$

The output power is a result of multiplying the rectifier input power by the characterized rectifier efficiency

$$P_{\text{out}} = \eta_{\text{rect}} P_{\text{rect}}. \tag{26}$$

The proposed WPT system model can accurately derive the power at each block by using the known and design parameters in Table II. So, the power loss and system efficiency can be calculated by the two corresponding power values. For instance, the power loss on the TX coil and TX matching network is

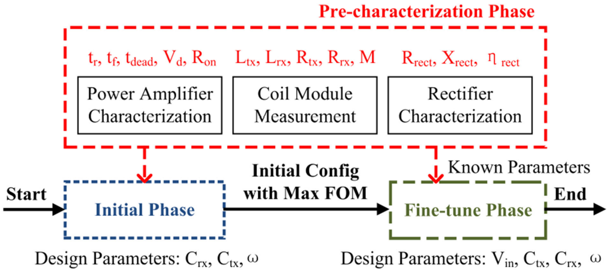

Fig. 10. Flowchart of the design methodology.

$(P_{pa} - P_{rx})$, the power loss on the RX coil and RX matching network is $(P_{rx} - P_{rect})$, and the system and coil efficiencies can be calculated based on (2) and (3) respectively. Therefore, this model is capable of conducting system-level optimization by tuning the design parameters analytically, instead of building a complete prototype and conducting massive measurements.

B. Practical Design Methodology

One of the challenges in designing WPT systems is the lack of practical design methodologies. There are multiple parameters, such as the input voltage, the TX/RX coil matching capacitance, and the operating frequency, involved in determining the system efficiency. These parameters are coupled with each other, so it is unfeasible to tune them one by one. Conventionally, the trial-and-error method is used to conduct measurements under all the combinations of parameters within the ranges of interests, which is time-consuming and costly. With the help of the improved WPT model, a novel design methodology is introduced to overcome these challenges.

The entire design process is divided into three phases: the *precharacterization phase*, the *initial phase*, and the *fine-tune phase*. This design flow is shown in Fig. 10.

1) The *precharacterization phase* aims to obtain the "known parameters" (see Table II) of the provided blocks, including the power amplifier, the coil module, and the rectifier. These parameters are accessible from the device's datasheet, oscilloscope, or impedance analyzer measurements, and the characterization method discussed in Section III. The precharacterized data can be collected into the lookup tables.
2) After the characterization on provided blocks, it is critical to set proper initial values for the design parameters. In the *initial phase*, the WPT model can be simplified by neglecting the switching and dead time losses of the power amplifier, and the higher order frequency harmonics. Then, the simplified system efficiency becomes

$$\begin{aligned}\eta_{\text{sys,initial}} &= \eta_{\text{rect}} \frac{P_{\text{rect}}^{(1)}}{P_{\text{in,cond}}^{(1)}} \\ &= \eta_{\text{rect}} \frac{R_{\text{rect}}^{(1)}}{R_{\text{rx}}^{(1)} + R_{\text{rect}}^{(1)}} \frac{R_{\text{rx\_ref}}^{(1)}}{R_{\text{s}} + R_{\text{tx}}^{(1)} + R_{\text{rx\_ref}}^{(1)}}. \quad (27)\end{aligned}$$

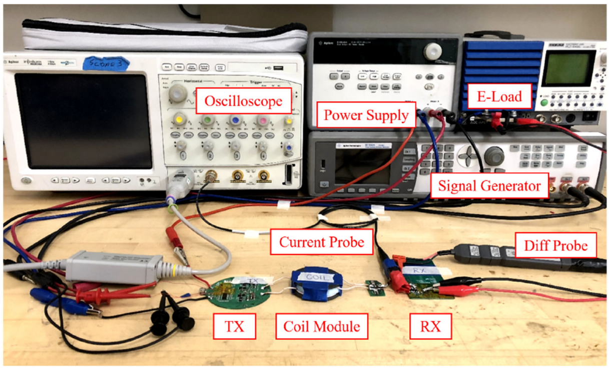

Fig. 11. Photograph of the experimental prototype.

Note that η_{rect}, R_{s}, $R_{\text{rx}}^{(1)}$, and $R_{\text{tx}}^{(1)}$ are constants unrelated to the design parameters. Therefore, a figure of merit (FOM) is defined to find the initial values for the design parameters as

$$\text{FOM} = \frac{R_{\text{rect}}^{(1)}}{A + R_{\text{rect}}^{(1)}} \cdot \frac{R_{\text{rx\_ref}}^{(1)}}{B + R_{\text{rx\_ref}}^{(1)}} \quad (28)$$

where $A = R_{\text{rx}}^{(1)}$ and $B = R_{\text{s}} + R_{\text{tx}}^{(1)}$ are both predetermined constants. In this simplified condition, the goal is to maximize the FOM at the fundamental frequency. Based on (5) and (11), the FOM is determined by C_{rx}, C_{tx}, and ω. Other design parameters, such as V_{in}, are mainly set to provide sufficient power capability for the WPT system.

3) Finally, the full WPT model is included in the *fine-tune phase*. All the design parameters are tuned in fine steps based on the initial values. So, the optimizations can quickly converge to the actual optimal efficiency point.

V. EXPERIMENT AND VALIDATION

An experimental prototype was implemented to validate the proposed model. It was designed based on a real WPT system for cell phone products. In addition, the design methodology to optimize the system parameters is also validated using this prototype.

The experimental setup is depicted in Fig. 11. The coil module consists of one TX coil and one RX coil. Two coils are aligned with each other by the center point and have 3-mm spacing in the vertical distance. The TX coil is built based on the standard A11 type from the Qi specification [5]. The RX coil is routed by 15-turn solid copper wires, and the physical dimensions are 38 mm × 32 mm. Both the TX and RX coils are assembled with magnetic ferrites. The matching capacitance is 400 nF for the TX coil and 200 nF for the RX coil. The detailed electrical specifications of this coil module are listed in Table I (WPT system coil for validation). On the TX printed circuit board (PCB) board, a full-bridge power amplifier is implemented by four N-channel MOSFETs (AON7544) and two gate drivers (NCP81151). The dc voltage for the TX board is provided by a dual-output power supply (Agilent E3648A). Since the proposed modeling method focuses on the power flow path of the WPT

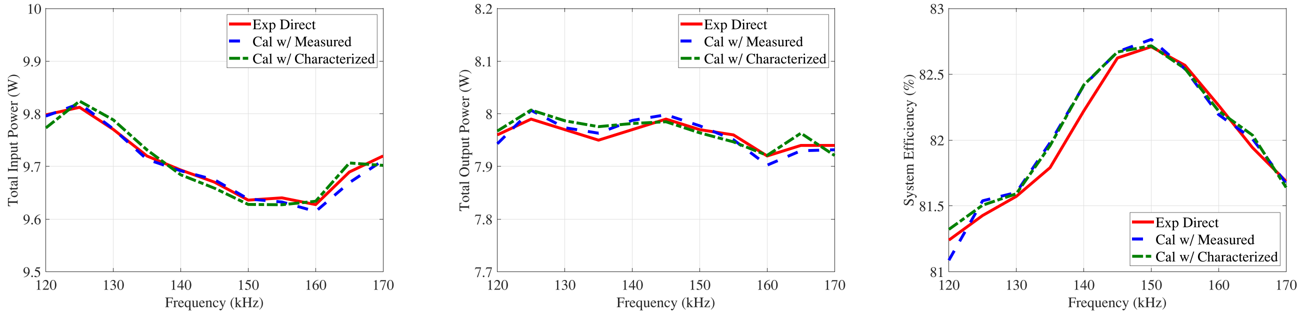

(a) (b) (c)

Fig. 12. Comparison of input powers, output powers, and system efficiencies between the experiment and calculation results. The rated output power is 8 W with less than 0.1-W variation in actual measurement, and the operating frequency varies from 120 to 170 kHz. (a) Total input power. (b) Total output power. (c) System efficiency.

system, the experiment is also designed to remove the impact of other nonpower-path circuits. Therefore, one output of the power supply is dedicated to the power flow path. The nonpower-path devices, such as the gate driver, are powered separately by the other output. The gate drivers are controlled by two inverted channels from a signal generator (Agilent 81150 A), where two square waves with the same frequency and 180° out phase are generated. On the RX PCB board, a full-wave rectifier is implemented by four Schottky diodes (SBR3U40P1) and two 10-μF smoothing capacitors. The dc output is connected to an electrical load (KIKUSUI PLZ164WL), which operates in the 8.67-Ω constant-resistance mode. The RX output voltage is fixed to 8.33 V, and the rated output power is 8 W. The system efficiency of this experimental setup is calculated based on the dc powers measured at the input and output sides ($P_{\text{in}}/P_{\text{out}}$). The intermediate ac powers, such as the power amplifier output power (P_{pa}) and the rectifier input power (P_{rect}), are measured in the time domain by an oscilloscope (Agilent MSO8104A) with differential and current clamp probes.

A. Validation on Characterization and Modeling

In order to validate both the rectifier characterization method and the improved WPT model, three types of results have been compared: 1) the direct measured power and system efficiency from this experimental setup: "Exp Direct"; 2) the calculated result with measured rectifier impedance: "Cal w/ Measured"; it validated this improved WPT model; and 3) the calculated result with characterized rectifier impedance: "Cal w/ Characterized"; by using the fitted rectifier impedance curve (the solid line in Fig. 7), it validated the accuracy of this rectifier characterization method.

The calculations, based on (16), (26), and (2) the experiment results of input power P_{in}, output power P_{out}, and system efficiency η_{sys} versus the operating frequency are plotted in Fig. 12. The three types of results have good correlation with each other. The highest η_{sys} is achieved at 150 kHz, with the input voltage $V_{\text{in}} = 8.52$ V. The improved WPT model does not require any impractical assumptions used in the conventional modeling methods and can find the peak efficiency point across a wide frequency range.

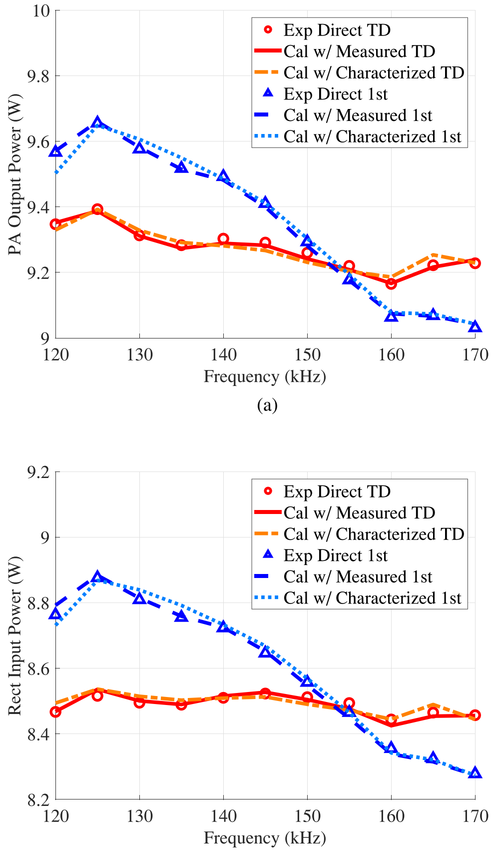

(a)

(b)

Fig. 13. Comparison of intermediate ac power between experiment and calculation results. "TD" implies the total time-domain result. "1st" implies that only fundamental frequency is considered. (a) Power amplifier output power P_{pa}. (b) Rectifier input power P_{rect}.

Since this model is built on the basis of frequency harmonic analysis, it is important to validate the accuracy of the calculated power distributed on each frequency component. The comparison of intermediate ac powers, including P_{pa} and P_{rect}, is shown in Fig. 13. For experiment, the time-domain result ("Exp TD") is obtained by multiplying the measured voltage and current directly, and the fundamental frequency result ("Exp 1st") is

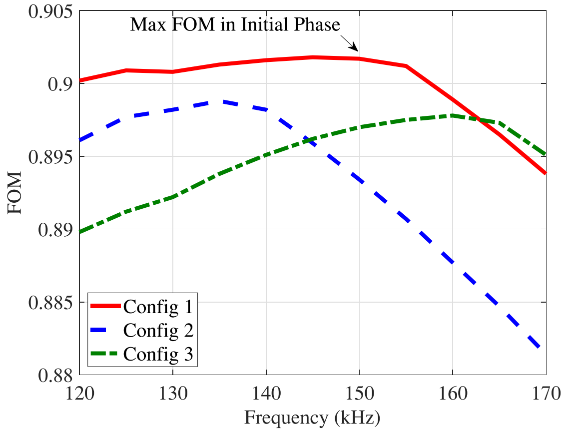

Fig. 14. FOM calculation in the *initial phase* of the design methodology.

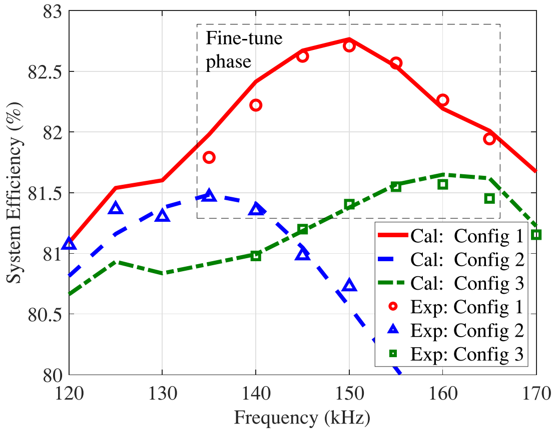

Fig. 15. System efficiency comparison in the *fine-tune phase* of the design methodology.

extracted from the FFT processed time-domain waveforms. For calculation, P_{pa} and P_{rect} distributed on each frequency component are calculated based on (23) and (25). The time-domain result ("Cal TD") includes the three most significant components: the fundamental, third-order, and fifth-order harmonics. The fundamental frequency result ("Cal 1st") only considers the fundamental component. The good agreement between experiment and calculation validates the improved model in both time and frequency domains. Additionally, it shows that this model can not only estimate the end-to-end system efficiency, but also provide the accurate power loss of each block in a WPT system. As a result, it provides more flexibility to set different loss thresholds for the critical blocks and improve the thermal design. The configuration with the maximum FOM achieves the best system efficiency.

B. Validation on Design Methodology

The design methodology is validated using the same experimental prototype, so the *precharacterization phase* has already been conducted. In the *initial phase*, three different configurations of the matching capacitance are investigated.

1) Config 1 : $C_{\mathrm{tx}} = 400$ nF and $C_{\mathrm{rx}} = 200$ nF.
2) Config 2 : $C_{\mathrm{tx}} = 400$ nF and $C_{\mathrm{rx}} = 300$ nF.
3) Config 3 : $C_{\mathrm{tx}} = 300$ nF and $C_{\mathrm{rx}} = 200$ nF.

The FOM for each configuration is calculated based on (28) by sweeping the operating frequency from 120 to 170 kHz, as shown in Fig. 14. The global maximum FOM is achieved with "Config 1" at around 150 kHz. To validate the effectiveness of the FOM, these configurations are intentionally kept the same in the *fine-tune phase*. Then, the other design parameters are tuned based on the initial values set by the local maximum FOM of each configuration. Fig. 15 compares the system efficiencies from both calculations and experiments. The trend of system efficiency is very close to the predictions based on the FOM, which implies that the FOM can effectively determine the proper initial values for the design parameters. Note that the system efficiency is also affected by other blocks. Therefore, it is necessary to tune the design parameters in fine steps for the optimal system efficiency. The actual calculations in the *fine-tune phase* is from 135 to 165 kHz for all configurations, which is illustrated by the dashed line box in Fig. 15. The final optimal configurations are: $C_{\mathrm{tx}} = 400$ nF, $C_{\mathrm{rx}} = 200$ nF, $V_{\mathrm{in}} = 8.52$ V, and operating frequency at 150 kHz.

VI. CONCLUSION

In this article, the impractical assumptions of the existing WPT system modeling methods are investigated by circuit simulations. To avoid the pure resistance load assumption, an accurate rectifier characterization method is proposed to provide a realistic load condition. On the basis of the characterized rectifier impedance, a novel system-level WPT model is presented instead of only focusing on the coil-to-coil part. The improved model considers both the fundamental frequency and higher order harmonics, which can effectively eliminate the inaccuracy caused by FHA at off-resonance conditions. Good performance of the model is validated by experimental measurements in both time and frequency domains. The result shows that it can accurately estimate the system efficiency and power loss at each interior block. With the assistance of this model, a practical methodology is introduced to efficiently optimize the design parameters of a WPT system.

APPENDIX

Based on the small-signal analysis, the derivations of (6) is described in the following procedures. All variables are defined the same as Fig. 4.

1) *Define the source voltage v_s with a perturbation:* Assume that the source voltage v_{s} consists of a sinusoidal wave v_1 and a small-signal perturbation Δv_{p}: $v_{\mathrm{s}} = v_1 + \Delta v_{\mathrm{p}}$, where $|v_1| = V_1$, $|\Delta v_{\mathrm{p}}| = V_{\mathrm{p}}$ with $V_{\mathrm{p}} \ll V_1$.
2) *Calculate the output voltage v_{dc}:* Using the nonlinear switching functions S and ΔS defined in Section III, the mapping relationship between the input and output sides of the rectifier can be expressed as

$$\begin{cases} v_{\mathrm{dc}} = (S + \Delta S) \cdot v_{\mathrm{ac}} \\ i_{\mathrm{ac}} = (S + \Delta S) \cdot i_{\mathrm{dc}}. \end{cases} \tag{29}$$

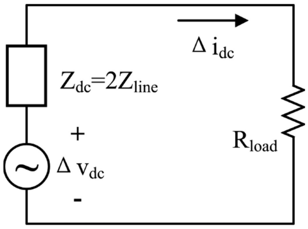

Fig. 16. Thevenin equivalent circuit for the output side of the rectifier.

The input voltage v_{ac} and output voltage v_{dc} are calculated by combining the source voltage v_{s}, the switching functions $(S + \Delta S)$, and the line impedance Z_{line} as

$$\begin{aligned} v_{\text{ac}} &= v_{\text{s}} - i_{\text{ac}} \cdot Z_{\text{line}} \\ &= (v_1 + \Delta v_{\text{p}}) - (S + \Delta S) \cdot i_{\text{dc}} \cdot Z_{\text{line}} \end{aligned} \tag{30}$$

$$\begin{aligned} v_{\text{dc}} &= (S + \Delta S) \cdot v_{\text{ac}} \\ &= (S + \Delta S) \cdot [(v_1 + \Delta v_{\text{p}}) - (S + \Delta S) \cdot i_{\text{dc}} \cdot Z_{\text{line}}] \\ &\approx S \cdot v_1 + \Delta S \cdot v_1 + S \cdot \Delta v_{\text{p}} \\ &\quad - S^2 \cdot i_{\text{dc}} \cdot Z_{\text{line}} - 2S \cdot \Delta S \cdot i_{\text{dc}} \cdot Z_{\text{line}}. \end{aligned} \tag{31}$$

Note that two terms $(\Delta S \cdot \Delta v_{\text{p}})$ and $(\Delta S^2 \cdot i_{\text{dc}} \cdot Z_{\text{line}})$ are neglected because they involve the product of two small variation values ΔS and Δv_{p}.

The first term $(S \cdot v_1)$ is caused by the main wave. The second and third terms, $(\Delta S \cdot v_1)$ and $(S \cdot \Delta v_{\text{p}})$, are related to the perturbation. The other terms are affected by the mutual effects of both signals, because the output current i_{dc} contains both main wave and perturbation components. In order to decouple the mutual effects, i_{dc} can be approximated to the dc component of the load current I_{d}. Then, the output voltage v_{dc} can be expressed by the main wave component $v_{\text{dc, 1}}$ and the perturbation component Δv_{dc}

$$v_{\text{dc}} = v_{\text{dc, 1}} + \Delta v_{\text{dc}} \tag{32}$$

where

$$\begin{cases} v_{\text{dc, 1}} \approx S \cdot v_1 - S^2 \cdot I_{\text{d}} \cdot Z_{\text{line}} \\ \Delta v_{\text{dc}} \approx \Delta S \cdot v_1 + S \cdot \Delta v_{\text{p}} - 2S \cdot \Delta S \cdot I_{\text{d}} \cdot Z_{\text{line}}. \end{cases} \tag{33}$$

3) *Calculate the output current i_{dc}:* Similar with v_{dc}, the output current i_{dc} consists of the main wave component $i_{\text{dc,1}}$ and the perturbation component Δi_{dc}

$$i_{\text{dc}} = i_{\text{dc,1}} + \Delta i_{\text{dc}}. \tag{34}$$

The dc component of i_{dc} is denoted as I_{d}, which can be simply determined by the rated output power P_{out} and the load impedance R_{load}: $I_{\text{d}} = \sqrt{P_{\text{out}}/R_{\text{load}}}$.

The ac components are calculated based on the Thevenin equivalent circuit representing the output side of the rectifier, as shown in Fig. 16. The voltage source of this equivalent circuit can be either $v_{\text{dc,1}}$ or Δv_{dc}. Correspondingly, the current is $i_{\text{dc,1}}$ or Δi_{dc}. The source impedance Z_{dc} is mapped from the ac-side line impedance Z_{line}. For the single-phase rectifier without overlap period, Z_{dc} approximately equals $2Z_{\text{line}}$ [24], [25]. Then, the ac components of the output current can be calculated as

$$i_{\text{dc,1}} = \frac{v_{\text{dc,1}}}{Z_{\text{dc}} + R_{\text{load}}} = \frac{S \cdot v_1 - S^2 \cdot I_{\text{d}} \cdot Z_{\text{line}}}{2Z_{\text{line}} + R_{\text{load}}} \tag{35}$$

$$\Delta i_{\text{dc}} = \frac{\Delta v_{\text{dc}}}{Z_{\text{dc}} + R_{\text{load}}} = \frac{\Delta S v_1 + S \Delta v_{\text{p}} - 2S \Delta S I_{\text{d}} Z_{\text{line}}}{2Z_{\text{line}} + R_{\text{load}}}. \tag{36}$$

4) *Map the output current to the ac-side input current i_{ac}:* Based on the mapping relationship, the ac-side input current i_{ac} can be calculated from the output current as

$$i_{\text{ac}} = (S + \Delta S) \cdot i_{\text{dc}} = (S + \Delta S) \cdot (i_{\text{dc, 1}} + \Delta i_{\text{dc}}). \tag{37}$$

To calculate the input impedance of the rectifier, only the perturbation component Δi_{ac} is needed. So, Δi_{ac} is extracted from (37) and expressed as

$$\begin{aligned} \Delta i_{\text{ac}} &= \Delta S \cdot i_{\text{dc,1}} + S \cdot \Delta i_{\text{dc}} \\ &= \frac{2S \Delta S v_1 + S^2 \Delta v_{\text{p}} - 3S^2 \Delta S I_{\text{d}} Z_{\text{line}}}{2Z_{\text{line}} + R_{\text{load}}}. \end{aligned} \tag{38}$$

The perturbation component of the input voltage Δv_{ac} is

$$\Delta v_{\text{ac}} = \Delta v_p - \Delta S \cdot I_{\text{d}} \cdot Z_{\text{line}}. \tag{39}$$

Finally, the input impedance of the rectifier can be calculated by the ratio of perturbation voltage and current at the input side $\Delta v_{\text{ac}}/\Delta i_{\text{ac}}$, as shown in (6).

REFERENCES

[1] C. C. Mi, G. Buja, S. Y. Choi, and C. T. Rim, “Modern advances in wireless power transfer systems for roadway powered electric vehicles,” *IEEE Trans. Ind. Electron.*, vol. 63, no. 10, pp. 6533–6545, Oct. 2016.

[2] S. Li and C. C. Mi, “Wireless power transfer for electric vehicle applications,” *IEEE J. Emerg. Sel. Topics Power Electron.*, vol. 3, no. 1, pp. 4–17, Mar. 2015.

[3] X. Lu, P. Wang, D. Niyato, D. I. Kim, and Z. Han, “Wireless charging technologies: Fundamentals, standards, and network applications,” *IEEE Commun. Surv. Tut.*, vol. 18, no. 2, pp. 1413–1452, Apr.–Jun. 2016.

[4] X. Mou and H. Sun, “Wireless power transfer: Survey and roadmap,” in *Proc. 81st IEEE Veh. Technol. Conf.*, 2015, pp. 1–5.

[5] D. Van Wageningen and T. Staring, “The QI wireless power standard,” in *Proc. 14th Int. IEEE Power Electron. Motion Control Conf.*, 2010, pp. S15–25.

[6] J. Schneider, *SAE J2954 Overview and Path Forward*. Warrendale, PA, USA: SAE Int., 2013.

[7] J. Cho, J. Sun, H. Kim, J. Fan, Y. Lu, and S. Pan, “Coil design for 100 kHz and 6.78 MHz WPT system: Litz and solid wires and winding methods,” in *Proc. IEEE Int. Symp. Electromagn. Compat. Signal/Power Integrity*, 2017, pp. 803–806.

[8] C.-S. Wang, G. A. Covic, and O. H. Stielau, “Power transfer capability and bifurcation phenomena of loosely coupled inductive power transfer systems,” *IEEE Trans. Ind. Electron.*, vol. 51, no. 1, pp. 148–157, Feb. 2004.

[9] Y. H. Sohn, B. H. Choi, E. S. Lee, G. C. Lim, G.-H. Cho, and C. T. Rim, “General unified analyses of two-capacitor inductive power transfer systems: Equivalence of current-source SS and SP compensations,” *IEEE Trans. Power Electron.*, vol. 30, no. 11, pp. 6030–6045, Nov. 2015.

[10] M. Fu, Z. Tang, and C. Ma, “Analysis and optimized design of compensation capacitors for a megahertz WPT system using full-bridge rectifier,” *IEEE Trans. Ind. Inform.*, vol. 15, no. 1, pp. 95–104, Jan. 2019.

[11] Y. Guo, L. Wang, Y. Zhang, S. Li, and C. Liao, “Rectifier load analysis for electric vehicle wireless charging system,” *IEEE Trans. Ind. Electron.*, vol. 65, no. 9, pp. 6970–6982, Sep. 2018.

[12] Y. Zhang, T. Kan, Z. Yan, and C. C. Mi, “Frequency and voltage tuning of series-series compensated wireless power transfer system to sustain rated power under various conditions,” *IEEE J. Emerg. Sel. Topics Power Electron.*, vol. 7, no. 2, pp. 1311–1317, Jun. 2019.

[13] C. Oeder, A. Bucher, J. Stahl, and T. Duerbaum, “A comparison of different design methods for the multiresonant LLC converter with capacitive output filter,” in *Proc. IEEE 12th Workshop Control Model. Power Electron.*, 2010, pp. 1–7.

[14] M. K. Kazimierczuk and D. Czarkowski, *Resonant Power Converters*. Hoboken, NJ, USA: Wiley, 2012.

[15] L. Jianyu, T. Houjun, and G. Xin, “Frequency splitting analysis of wireless power transfer system based on t-type transformer model,” *Elektronika ir Elektrotechnika*, vol. 19, no. 10, pp. 109–113, 2013.

[16] T. Kan, T.-D. Nguyen, J. C. White, R. K. Malhan, and C. C. Mi, “A new integration method for an electric vehicle wireless charging system using LCC compensation topology: Analysis and design,” *IEEE Trans. power Electron.*, vol. 32, no. 2, pp. 1638–1650, Feb. 2017.

[17] S. Y. Choi, J. Huh, W. Y. Lee, and C. T. Rim, “Asymmetric coil sets for wireless stationary EV chargers with large lateral tolerance by dominant field analysis,” *IEEE Trans. Power Electron.*, vol. 29, no. 12, pp. 6406–6420, Dec. 2014.

[18] Y. Zhang, K. Chen, F. He, Z. Zhao, T. Lu, and L. Yuan, “Closed-form oriented modeling and analysis of wireless power transfer system with constant-voltage source and load,” *IEEE Trans. Power Electron.*, vol. 31, no. 5, pp. 3472–3481, May 2016.

[19] P. Grzejszczak and R. Barlik, “The description of turn-off process and evaluation of switching power losses in the ultra fast power MOSFET,” *Power Electron. Drives*, vol. 1, no. 1, pp. 55–67, 2016.

[20] P. Smeets, “First harmonic approximation—Power transfer deviation for resonant LLC converters,” ZeoN PowerTec Tech. Note, 2017.

[21] S. Ladan and K. Wu, “Nonlinear modeling and harmonic recycling of millimeter-wave rectifier circuit,” *IEEE Trans. Microw. Theory Techn.*, vol. 63, no. 3, pp. 937–944, Mar. 2015.

[22] J. Sun and K. J. Karimi, “Small-signal input impedance modeling of line-frequency rectifiers,” *IEEE Trans. Aerosp. Electron. Syst.*, vol. 44, no. 4, pp. 1489–1497, Oct. 2008.

[23] J. Sun, “Small-signal methods for ac distributed power systems—A review,” *IEEE Trans. Power Electron.*, vol. 24, no. 11, pp. 2545–2554, Nov. 2009.

[24] Q. Lei, M. Shen, V. Blasko, and F. Z. Peng, “A generalized input impedance model of three phase diode rectifier,” in *Proc. 28th Annu. IEEE Appl. Power Electron. Conf. Expo.*, 2013, pp. 2655–2661.

[25] M. Sakui, H. Fujita, and M. Shioya, “A method for calculating harmonic currents of a three-phase bridge uncontrolled rectifier with dc filter,” *IEEE Trans. Ind. Electron.*, vol. 36, no. 3, pp. 434–440, Aug. 1989.

[26] T. Kuphaldt, *Lessons in Electric Circuits—Semiconductors*, vol. III, 5th Ed., Open Book Project, 2009.

[27] W. Zhong and S. Hui, “Maximum energy efficiency tracking for wireless power transfer systems,” *IEEE Trans. Power Electron.*, vol. 30, no. 7, pp. 4025–4034, Jul. 2015.

[28] Y. Yang, W. Zhong, S. Kiratipongvoot, S.-C. Tan, and S. Y. R. Hui, “Dynamic improvement of series–series compensated wireless power transfer systems using discrete sliding mode control,” *IEEE Trans. Power Electron.*, vol. 33, no. 7, pp. 6351–6360, Jul. 2018.

[29] W. Zhong and S. R. Hui, “Charging time control of wireless power transfer systems without using mutual coupling information and wireless communication system,” *IEEE Trans. Ind. Electron.*, vol. 64, no. 1, pp. 228–235, Jan. 2017.

[30] ROHM Semiconductor, “Switching regulator IC series: Calculation of power loss (synchronous),” 2016. Accessed: Apr. 17, 2019. [Online]. Available: http://rohmfs.rohm.com/en/products/databook/applinote/ic/power/switching_regulator/power_loss_appli-e.pdf

Jingdong Sun (Student Member, IEEE) received the B.S. degree in electronic information and communications from the Huazhong University of Science and Technology, Wuhan, China in 2014, and the M.S. degree in electrical engineering in 2016 from the Missouri University of Science and Technology, Rolla, MO, USA, where he is currently working toward the Ph.D. degree in electrical engineering.

His research interests include device modeling for electromagnetic interference and power distribution network applications, signal/power integrity, and wireless power transfer.

Mr. Sun was the recipient of the IEEE EMC Hardware Design Award in 2015.

Jonghyun Cho (Member, IEEE) received the B.S., M.S., and Ph.D. degrees in electrical engineering from the Korea Advanced Institute of Science and Technology (KAIST), Daejeon, South Korea, in 2008, 2010, and 2013, respectively.

He was a Postdoctoral Researcher with KAIST until the end of 2014. In 2015, he joined the Electromagnetic Compatibility Laboratory, Missouri University of Science and Technology, Rolla, MO, USA, as a Visiting Assistant Research Professor and continued research at the field of signal integrity (SI) and power integrity (PI). In 2017, he joined Rambus Inc., Sunnyvale, CA, USA, where he is working on SI and PI of DDR4/DDR5 buffer chip.

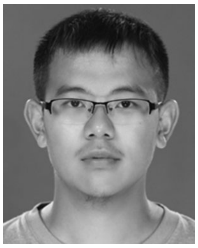

Anfeng Huang (Student Member, IEEE) was born in Guangxi, China, in July 1992. He received the B.E. and M.S. degrees from Xidian University, Xi’an, China, in 2014 and 2017, respectively. He is currently working toward the Ph.D. degree in electrical engineering with the Electromagnetic Compatibility Laboratory, Missouri University of Science and Technology, Rolla, MO, USA.

His current research interests include wireless power transfer systems, ferrite characterization, and advance measurement.

Hongseok Kim (Member, IEEE) received the Ph.D. degree in electrical engineering from the Korea Advanced Institute of Science and Technology, Daejeon, South Korea, in 2017.

He is currently a Visiting Assistant Research Professor with the Electromagnetic Compatibility (EMC) Laboratory, Missouri University of Science and Technology, Rolla, MO, USA. His current research interests include EMC modeling, analysis, and design of automotive power electronics, including wireless charging systems and motor drive systems.

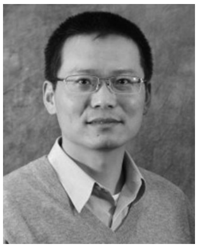

Jun Fan (Fellow, IEEE) received the B.S. and M.S. degrees in electronic engineering from Tsinghua University, Beijing, China, in 1994 and 1997, respectively, and the Ph.D. degree in electrical engineering from the University of Missouri–Rolla, Rolla, MO, USA, in 2000.

From 2000 to 2007, he was a Consultant Engineer with NCR Corporation, San Diego, CA, USA. In July 2007, he joined the Missouri University of Science and Technology (Missouri S&T) (formerly University of Missouri–Rolla), where he is currently the Cynthia Tang Missouri Distinguished Professor in Computer Engineering and the Director of the Electromagnetic Compatibility (EMC) Laboratory. His research interests include signal integrity and electromagnetic interference (EMI) designs in high-speed digital systems, dc power-bus modeling, intrasystem EMI and RF interference, printed circuit board noise reduction, differential signaling, and cable/connector designs.

Dr. Fan also serves as the Director of the National Science Foundation Industry/University Cooperative Research Center for Electromagnetic Compatibility and a Senior Investigator of the Missouri S&T Material Research Center. In the IEEE EMC Society, he served as the Chair of the TC-9 Computational Electromagnetics Committee from 2006 to 2008, the Chair of the Technical Advisory Committee from 2014 to 2016, and a Distinguished Lecturer in 2007 and 2008. He is an Associate Editor for the IEEE TRANSACTIONS ON ELECTROMAGNETIC COMPATIBILITY and the IEEE EMC MAGAZINE. He received the IEEE EMC Society Technical Achievement Award in August 2009.